



Cutting-down the energy consumption of electrohydrodynamic drying by optimizing mesh collector electrode

Kamran Iranshahi ^{a, b}, Alex Martynenko ^c, Thijs Defraeye ^{a, c, *}

^a Empa, Swiss Federal Laboratories for Materials Science and Technology, Laboratory for Biomimetic Membranes and Textiles, Lerchenfeldstrasse 5, CH-9014, St. Gallen, Switzerland

^b Department of Mechanical Engineering, Politecnico di Milano, Via La Masa 34, 20100, Milan, Italy

^c Department of Engineering, Dalhousie University, Faculty of Agriculture, Truro, Nova Scotia, Canada

ARTICLE INFO

Article history:

Received 27 January 2020

Received in revised form

2 June 2020

Accepted 16 June 2020

Available online 27 June 2020

Keywords:

EHD

Dehydration

Food drying

Simulation

Exergy analysis

Ionic wind

ABSTRACT

Drying is one of the most energy-intensive processes in the multiple industries, due to the high latent heat required to evaporate the water, which is often done by employing hot-air drying. Electrohydrodynamic (EHD) drying is an alternative, innovative drying technology with large potential for industrial application and lower energy consumption. EHD drying is non-thermal, which makes this technology particularly suitable for drying of heat-sensitive biomaterials. A key bottleneck for EHD drying is the process scalability in order to uniformly dry large amounts of product, which is limited by the geometrical design of the collector electrode. To overcome this challenge, a recently introduced electrode configuration – a mesh collector – is further optimized in order to significantly reduce the energy consumption of the process. Exergy analysis was used to identify the energy conversion losses in ion production, ionic flow generation, and convective dehydration stages of fruit. As a result, a much more energy-efficient mesh configuration was designed. This improved design resulted in a similar drying rate as a normal mesh collector but showed a seven times smaller energy consumption. This upscalable, cleaner, and also much more energy-efficient EHD dryer design paves the way for industrial prototypes and pilot plants.

© 2020 The Authors. Published by Elsevier Ltd. This is an open access article under the CC BY license (<http://creativecommons.org/licenses/by/4.0/>).

1. Introduction

Drying is one of the oldest processing technologies with applications in food, agricultural, pharmaceutical, manufacturing, paper, polymer, and chemical industries. It is one of the oldest, and a very practical method for preserving biological materials, such as fruit and vegetables. It ensures longer storage life (shelf-life) of agricultural products to increase off-season availability and enables less energy-intensive transportation over large distances since most of the water is removed. Traditional drying methods, such as solar or forced-air drying, are cheap and easy to implement, but they have side-effects, such as long drying times and product contamination [1]. Industrial hot-air drying is the most commonly used technology but typically leads to loss of heat-sensitive compounds (e.g.,

vitamins, antioxidants), excessive shrinkage, and degradation of the color and flavor [2–4]. Advanced drying technologies, such as freeze-drying, are applied to avoid such quality loss. These are, however, often considered to be energy-intensive, costly, and less suitable for high-volume, low-value products, such as fruits and vegetables [1,5–7]. At the moment, a significant share of the global energy usage (annually about 95 EJ) is being consumed in the food sector [1]. Estimations show that drying consumes 10%–15% of the total energy consumption of all the food industries in developed countries [8]. This huge amount of energy consumption demands to employ more efficient drying technologies.

As an alternative to conventional drying methods, electrohydrodynamic (EHD) drying has been introduced. This promising, non-thermal technology has proven to be effective in dealing with the main issues of conventional dryers (e.g., cost/energy efficiency and product quality) by providing faster drying with less energy consumption [9–11]. In EHD drying, a high voltage is applied between the emitter and collector electrodes. Due to the large curvature of the emitter, air is locally ionized, resulting in a corona discharge. The generated ions are accelerated toward the grounded

* Corresponding author. Empa, Swiss Federal Laboratories for Materials Science and Technology, Laboratory for Biomimetic Membranes and Textiles, Lerchenfeldstrasse 5, CH-9014, St. Gallen, Switzerland.

E-mail addresses: kamran.iranshahi@empa.ch (K. Iranshahi), thijs.defraeye@empa.ch (T. Defraeye).

collector electrode by Coulomb force [12]. The movement of the charged particles transfers momentum to the air molecules through elastic and/or non-elastic collisions. Thereby, airflow is generated, which is called ionic wind (Fig. 1). EHD drying shows promising potential for industrial application as a sustainable drying technology with low energy consumption [11,13]. However, some issues have hindered the commercial implementation of this technology. For instance, little is still known about the exact contribution of different mechanisms of moisture transfer occurring during EHD drying, such as convection and electrically-induced mechanisms [9,14]. Moreover, challenges of scaling EHD drying from the lab-scale to industrial applications still need to be explored and evaluated.

Several investigations have been carried out to optimize the operating and geometrical parameters of emitter and collector electrodes. Most studies, however, apply a wire/needle-to-plate configuration [13,15]. This configuration has been argued to be unsuitable for drying large amounts of products simultaneously and uniformly at an industrial scale [15]. Recently, in a simulation-based study, Defraeye and Martynenko [10] compared different collector configurations and predicted significant improvements in the food drying rate by using a mesh instead of a plate collector. The mentioned study, however, represents mesh in a very idealized way as a homogeneous, highly porous grounded surface. To further develop and optimize the mesh collector design, a more realistic representation of the mesh would be beneficial in the computational model. Therefore, discrete computational modeling of the wire mesh is a next step in improving the collector design toward industrial applications.

In this study, we explored the impact of wire diameter, number of wires, and mesh open area on the electric field intensity, the resulting Coulomb force, the generated airflow, and the drying rate. As a second step, exergy analysis was performed for all the studied configurations to identify inefficiencies and losses. This information and quantified electrostatic parameters were used to optimize the mesh collector configuration. As an innovative step, this study is exploring one of the current challenges towards the upscaling of this technology which is simultaneous and uniform drying of a large amount of products with low energy consumption [16]. Accordingly, an optimal collector wire arrangement to minimize energy consumption has been proposed. First, this configuration enables the airflow to pass along each product and thereby avoids increase in air humidity, which negatively affects the drying process (Fig. 1). Second, the mesh enables the product to dry also from the bottom, leading to more uniform and faster drying [15]. Third, by grounding only a few number of collector wires, energy consumption decreases significantly. These features make the setup upscalable to large amounts of products.

2. Materials and methods

Convective EHD drying of fruit was modeled using the finite element method. The 2D model was composed of a wire-to-mesh configuration. All the used submodels for EHD, the associated airflow and drying process were validated previously. The details of the verification of the EHD model with experimental and analytical data are described in a previous work by Defraeye and Martynenko [10].

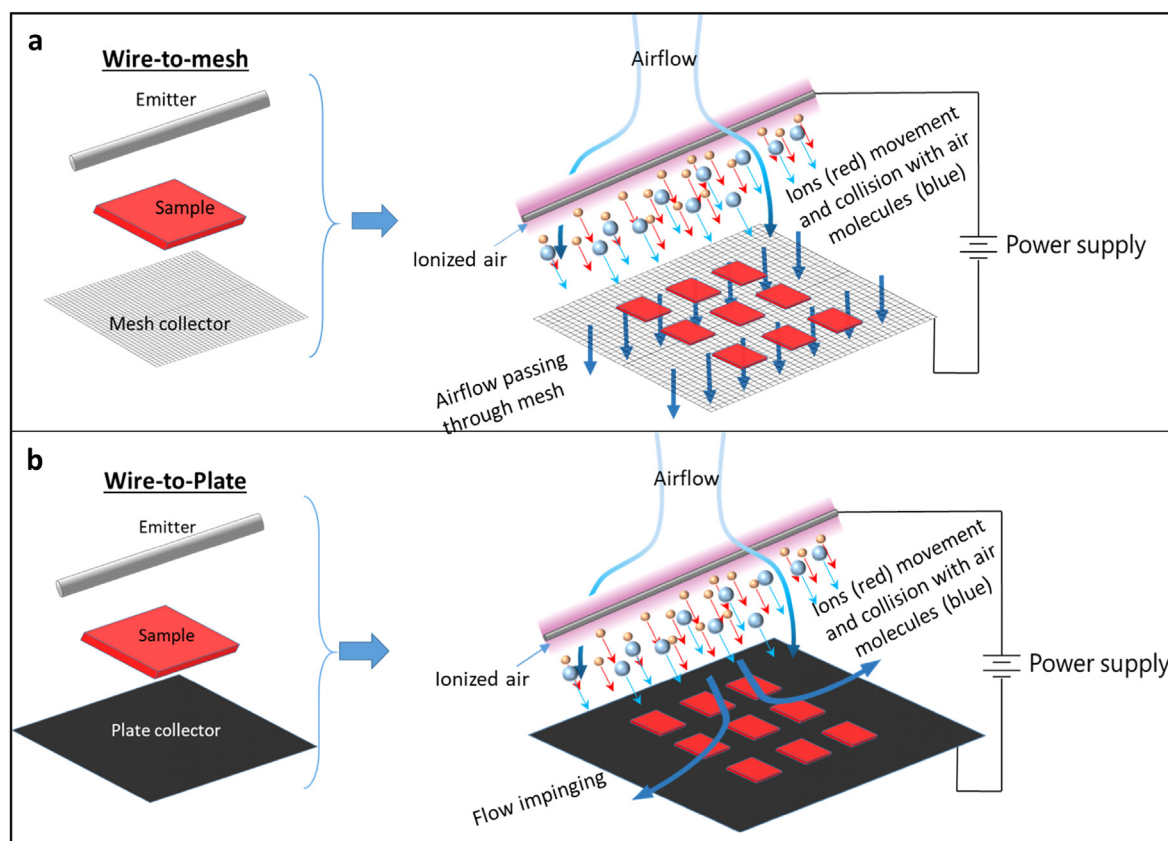


Fig. 1. Schematic of EHD dryer configurations: a) Wire-to-mesh configuration which enables the airflow to pass along each product and b) Wire-to-plate configuration with impinging airflow.

2.1. Multiphysics model

The multiphysics model aims to capture the following processes at play during EHD drying. By applying a positive high voltage (V) to the wire emitter, air is ionized and ions are produced in the vicinity of the emitter. These ions accelerate in a strong electric field to the grounded collector electrode and transfer momentum to the neutral air particles. This generates EHD-driven airflow toward the fruit sample by the so-called Coulomb force. The EHD airflow induces, in turn, convective heat and mass exchange with the fruit, which causes it to dry. To model these multiphysics processes, a three-step simulation procedure is applied. First, the electrostatic potential field and ion charge transport under the high-voltage field are simulated. Second, the resulting Coulomb force due to ion movement is used to calculate the airflow field. Third, the fruit dehydration due to convective heat and mass exchange is calculated. The specific physics and corresponding equations are described in the following paragraphs.

2.1.1. Electrostatics and space charge transport model

The electrical potential V [V] is linked to the electric field intensity \mathbf{E} [V m^{-1}] by Eq.(1). \mathbf{E} in the air and the fruit is described by Poisson's equation (Eq.(2)):

$$\mathbf{E} = -\nabla V \quad (1)$$

$$\nabla \cdot (\epsilon_0 \epsilon_r \mathbf{E}) = \rho_e \quad (2)$$

where ∇ and $\nabla \cdot$ indicate gradient and divergence operations, respectively. ρ_e [C m^{-3}] is the space charge density (SCD) of the ion/fluid medium, ϵ_0 [$\text{C V}^{-1} \text{m}^{-1}$] is the dielectric permittivity of vacuum ($8.854 \times 10^{-12} \text{C V}^{-1} \text{m}^{-1}$), and ϵ_r is the relative permittivity of the material. Note that in this paper inner product between vectors is denoted by point (for instance $\mathbf{A} \cdot \mathbf{B}$). The ion transport is described by the continuity equation for current density in the drift region (Ohm's law):

$$\nabla \cdot \mathbf{J} = 0 \quad (3)$$

$$\mathbf{J} = \mu_e \rho_e \mathbf{E} - D_i \nabla \rho_e + \rho_e \mathbf{u} \quad (4)$$

where \mathbf{J} [$\text{C m}^{-2} \text{s}^{-1}$] is the electric current density, μ_e [$\text{m}^2 \text{V}^{-1} \text{s}^{-1}$] is the ion mobility in the air ($1.8 \times 10^{-4} \text{m}^2 \text{V}^{-1} \text{s}^{-1}$), D_i [$\text{m}^2 \text{s}^{-1}$] is the diffusivity of the ions in the air, and \mathbf{u} [m s^{-1}] is the velocity vector for air. In the particular case of charged particles (i.e., not considering neutral particles), the drift motion produced by the electric field (first term on the right-hand side of Eq.(4)) is of the order of $\mu_e E \sim 10^{-1} - 10^2 \text{m s}^{-1}$ for EHD drying devices. This value is much higher than molecular diffusion, $D_i \sim 10^{-5} - 10^{-4}$ ($\nabla \rho_e$ in the domain is very low), or the advection gas motion which is of the order of $u \sim 10^{-4} - 5 \times 10^{-4} \text{m s}^{-1}$. Hence, the drift term is typically dominant, causing the equation to reduce to:

$$\mathbf{J} = \mu_e \rho_e \mathbf{E} \quad (5)$$

2.1.2. Airflow model

Airflow generation due to ion movement is calculated using the Navier–Stokes equation. To link the flow field to the electrostatics and space charge transport, the Coulomb body force (\mathbf{F}_e) is introduced into the momentum equation as a source term.

$$\rho_a \mathbf{u} \cdot \nabla \mathbf{u} = -\nabla p + \mu_a \nabla^2 \mathbf{u} + \mathbf{F}_e \quad (6)$$

$$\mathbf{F}_e = \rho_e \mathbf{E} \quad (7)$$

where ρ_a [kg m^{-3}] is the air density (1.20kg m^{-3} at 20°C), p [Pa] is the pressure, and μ_a [$\text{kg m}^{-1} \text{s}^{-1}$] is the dynamic viscosity of air ($1.81 \times 10^{-5} \text{kg m}^{-1} \text{s}^{-1}$ at 20°C).

2.1.3. Dehydration model of fruit tissue

The moisture transfer (i.e. dehydration) due to EHD could be attributed to several driving mechanisms [17]. However, the main enhancement of mass transfer is attributed to convection via EHD-generated airflow (ionic wind) [10,14]. In the current model, only convective moisture removal is taken into account. To this end, the convective heat transfer coefficient (CHTC) and convective mass transfer coefficient (CMTC) are determined from airflow calculations and are imposed as boundary conditions for fruit dehydration calculations. The material that is dehydrated is apple fruit. The following conservation equations are solved inside the fruit, further details are presented in Ref. [10].

$$\frac{\partial w_m}{\partial \psi} \frac{\partial \psi}{\partial t} + \nabla \cdot (-K_m \nabla \psi) = 0 \quad (8)$$

$$h_l \frac{\partial w_m}{\partial \psi} \frac{\partial \psi}{\partial t} + (c_{p,s} w_s + c_{p,l} w_m) \frac{\partial T}{\partial t} + \nabla \cdot (-h_l K_m \nabla \psi) + \nabla \cdot (-\lambda_{PM} \nabla T) = 0 \quad (9)$$

where ψ [Pa] is the water potential, w_s [kg m^{-3}] is the dry matter density (solid, 130kg m^{-3}) and w_m [kg m^{-3}] is the moisture content of the tissue. K_m [s] is the moisture permeability of the tissue ($8 \times 10^{-16} \text{s}$), h_l [J kg^{-1}] is the specific enthalpy of liquid water, λ_{PM} [$\text{W m}^{-1} \text{K}^{-1}$] is the thermal conductivity of the tissue (porous medium, $0.418 \text{W m}^{-1} \text{K}^{-1}$), $c_{p,s}$ and $c_{p,l}$ [$\text{J kg}^{-1} \text{K}^{-1}$] are the specific heat capacities of dry matter ($1634 \text{J kg}^{-1} \text{K}^{-1}$) and liquid water ($4182 \text{J kg}^{-1} \text{K}^{-1}$), respectively.

2.2. Computational system configuration

The computational system configuration in this study has a 2D geometry, consisted of a wire as the emitter electrode, a grounded mesh as the collector electrode, and a rectangular slice of apple ($L \times H = 10 \times 5 \text{mm}$) as the material that is dehydrated (Fig. 2), representing a long fruit stick. The EHD-generated airflow draws air at a temperature T_{ref} of 20°C and a relative humidity RH_{ref} of 30% from the inlet toward the fruit to be dried. These are typical conditions for convective fruit drying in the ambient environment. The emitter-collector distance and the voltage at the emitter wire are considered to be 20 mm and 20 kV, respectively. Other simulation conditions, as well as the computational model, are summarized in Fig. 2. As a further step toward a realistic model of the mesh collector, the size, number, and location of individual wires in the mesh have been considered. Including the wires discretely in the model should lead to a more precise simulation of the electric field intensity, Coulomb force, and resulting airflow around the drying material.

2.2.1. Effect of wire size and mesh open area

An important parameter of a mesh is the wire diameter. To quantify the impact of wire diameter on the EHD drying process, we simulated meshes with a constant open area but for varying wire diameters (d_w). This implies that by changing the diameter of wires, their number per unit area had to change to maintain the same open area. The wire spacing was chosen realistically, namely large enough to be transparent for airflow and small enough to support samples [18]. In this regard, three meshes with approximately 85%,

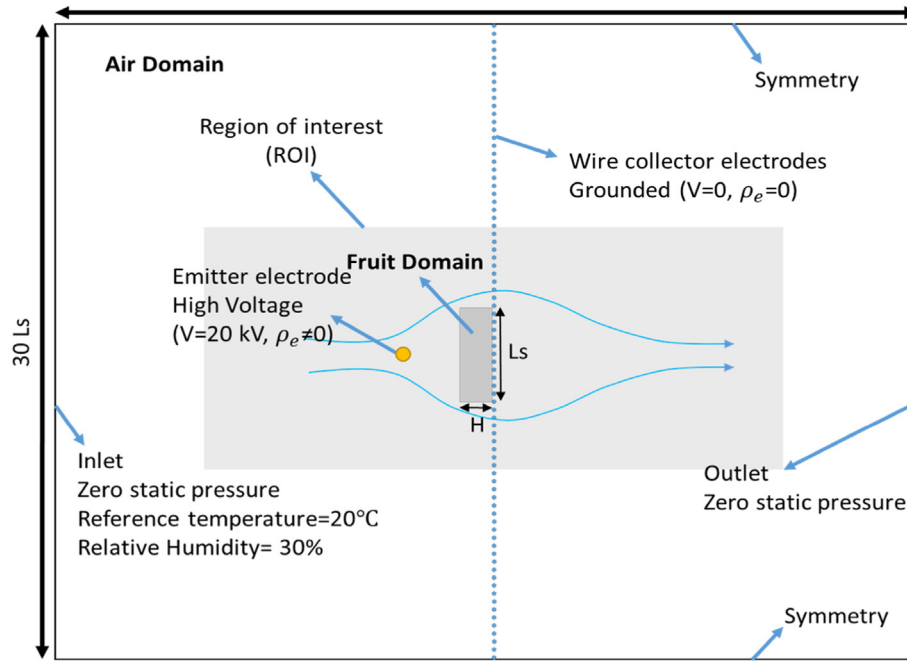


Fig. 2. Computational model and simulation conditions (figure not to scale).

70%, and 50% open area (porosity) were considered. Meshes with different open areas were compared to the ideal, homogeneous mesh which has an open area of 100%, as applied in Ref. [10]. The diameter and number of wires for different cases are presented in Table 1.

2.2.2. Optimization procedure and configurations

The objective of optimization was to minimize energy consumption by manipulating the electrostatic conditions of the mesh collector. Particularly, special arrangements of the grounded mesh wires were explored to concentrate the intensity of the electric field more closely to the sample. In other words, we aimed to increase the driver for EHD flow, the Coulomb force density, in the region of interest (ROI), namely the region in the vicinity of the fruit (defined in section 2.4). This can be achieved by increasing the local intensity of the electric field and guiding the charged particles into that specific region. To this end, the location of the grounded wires should satisfy both electrostatic and aerodynamic conditions. The first challenge for this optimization was to choose the lowest possible number of grounded wires to decrease input power while keeping average SCD and electric field strength as high as possible.

Table 1

Studied mesh configurations in terms of wire diameter and open area. The naming indicates first the percentage of the mesh open area and second the diameter of the wires.

Case name	Wire diameter d_w [μm]	Number of Wires	Open area [%]
Plate collector	-	-	0
Ideal Mesh	0	∞	100
P85_D1000	1000	23	85.2
P85_D500	500	46	85.2
P85_D300	300	75	85.5
P85_D240	240	97	85.1
P70_D1050	1050	46	70.4
P70_D500	500	97	70.3
P50_D1900	1900	46	50.2
P50_D900	900	97	50.3
P50_D500	500	175	50.2

Another challenge was to decrease the pressure loss by reducing the wire diameter within the limits of typical wires specification.

The first step to deal with these challenges was to find the optimum active area of the collector electrode. This has been done by increasing the number of the grounded wires. We started with only one grounded wire and then increased the number of wires to find the highest electric field intensity in the vicinity of the collector electrode. Increasing the number of grounded wires stopped when the evaluated metrics (e.g., energy consumption, drying time, etc.) showed little variation compared with the case of all grounded wires. Then, the optimum number of grounded wires has been chosen based on the trade-off between low drying time and low energy consumption. In this way, the lowest possible number of grounded wires has been found. As a next step, the locations of those optimum number of grounded wires were optimized to further enhance the performance. Different case studies for this optimization procedure are shown in Table 2.

2.3. Numerical simulations

This model was implemented in COMSOL Multiphysics (version 5.4a). Firstly, in order to obtain the critical SCD value on the emitter surface for corona formation, a parametric sweep was performed and the average of the resulting values based on different criteria (e.g. Ref. [18,19]) was selected. Having obtained the correct SCD, the electrical potential and space charge density distribution were solved at the same time as a stationary problem. Then, the steady-state turbulent airflow was solved. The stationary values of the convective mass and heat transfer coefficients on the fruit surface were obtained from the airflow and applied to the fruit boundaries. Finally, the transient dehydration process was simulated for 25 h, starting from the specified initial conditions.

A fully-coupled direct solver, based on the MUMPS (MULTifrontal Massively Parallel sparse direct Solver) algorithm and a segregated solver, relying on the PARDISO (PARallel Direct sparse Solver Interface) algorithm, were the solver schemes used for this simulation. The convergence threshold and other solver settings were

Table 2

Studied configurations of P85_D240 mesh for the minimization of energy consumption. For naming, the first part shows the mesh open area, the second part represents the number of grounded wires, and if grounded wires are in contact with the sample there will be a third part to indicate it.

Case study name	Grounded wire number	Not-grounded wire number	Grounded wire number in contact with sample
P85_2wire	2	95	0
P85_2wire_Contact	2	95	2
P85_3wire_Contact	3	94	1
P85_4wire	4	93	0
P99_4wire	4	0	0
P85_5wire_Contact	5	92	1
P85_6wire	6	91	0
P85_8wire	8	89	0
P85_16wire	16	81	0
P85_32wire	32	65	0
P85_64wire	64	33	0

determined based on sensitivity analysis in such a way that increasing the tolerance further did not alter the solution results anymore. Maximal time steps of 60 s, determined by a temporal sensitivity analysis, were applied combined with adaptive time-stepping. Grid sensitivity analysis was also carried out to ensure that grids were built properly for the air and fruit domains. To this end, we increased the resolution of the grids until the results did not change anymore. The grid consists of tetrahedral and quadrilateral finite elements which were refined toward electrode boundaries and the air–tissue interface for numerical accuracy enhancement. The total number of the elements varies from 336 181 to 726 122 depending on wire diameter and mesh open area.

2.4. Metrics to evaluate EHD drying performance

Several metrics were calculated in a specific region of interest (ROI): specifically a region close to the sample in which the most variation and largest gradients occur (Fig. 2). This was done because the phenomena of heat and mass transfer that play important roles in convective drying, take place close to the air–tissue boundary. For this study, a rectangle with a width of 10 sample length (L_s) and a length of $5L_s$ around the sample was arbitrarily considered as the region of interest. This specific area includes the sample, the emitter, and a part of the mesh collector close to the sample.

2.4.1. Drying time

To evaluate the drying time, the critical drying time was used. The critical drying time (t_{crit}) is defined as the time needed for the sample to reach the critical moisture content (w_{crit}) which is the averaged moisture content in the sample that corresponds to an equilibrium water activity below which no spoilage occurs [20]. w_{crit} was considered 37.8 kg m^{-3} for this study. Using t_{crit} enables us to have a simple way to compare different drying curves because a single value is obtained per drying process.

2.4.2. Mesh parameters

The open area of the mesh, β , can be defined as the ratio of open area to the total area:

$$\beta = \left(1 - \frac{d_w}{l}\right)^2 \quad (10)$$

where d_w is the wire diameter [m] and l is called the mesh length [m], which is the center-to-center distance between two wires.

2.4.3. Energy consumption

The energy consumption was calculated as a product of input power P_i [W] and critical drying time t_{crit} [s].

$$E = P_i \times t_{crit} \quad (11)$$

The input power is defined as:

$$P_i = \mathbf{V} \cdot \mathbf{I} \quad (12)$$

where \mathbf{I} is ionic current from emitter to collector which can be calculated for a unit length of the emitter, as [20,21]:

$$\mathbf{I} = \oint_{\text{emitter}} \mathbf{J} \, ds \cong 2\pi r_{\text{emitter}} \left(\sum_i \mu_{e_i} \rho_{e_i} \mathbf{E} \right)_{r_{\text{emitter}}} \quad (13)$$

In order to make it more general and sensible, the consumed energy [MJ] is defined per fresh fruit mass [kg] and it is called specific energy consumption (SEC) [MJ kg^{-1}].

2.4.4. Exergy analysis

Exergy is defined as the maximum work that can be extracted from a system when this system moves toward thermodynamic equilibrium with a reference environment [22]. In other words, it is simply the maximum available energy and is equivalent to the transformable work [23]. The exergy efficiency can be calculated using the following equation [23,24]:

$$\eta_E = \frac{Ex_{out}}{Ex_{in}} \times 100\% \quad (14)$$

Exergy analysis can be applied at both the entire process and sub-process levels, which enables us to evaluate the magnitudes and the location of the energy losses in the system [24]. Considering three main sub-processes of the entire process of EHD drying (Fig. 3), namely ion production, ionic flow generation, and convective dehydration, three exergy efficiencies have been defined. First, there is the electrical exergy efficiency η_E , which takes into account the corona (plasma) generation losses and it is determined as the ratio of discharged exergy (power) of the emitter (P_e) to the exergy (power) delivered by the energy source (P_i) [25]:

$$\eta_E = \frac{P_e}{P_i} \times 100\% \quad (15)$$

In this study, the input power (P_i) was calculated from Eq. (12) with \mathbf{V} equal to 20 kV, while the output power P_e was calculated from Eq. (16);

$$P_e = \oint_{\text{domain}} \mathbf{E} \cdot \mathbf{J} \, ds \quad (16)$$

Second, it is desirable to see how much of the power, discharged by the emitter is turned into air momentum. Here is the place to take into account the losses due to plastic collisions, ion dissipation,

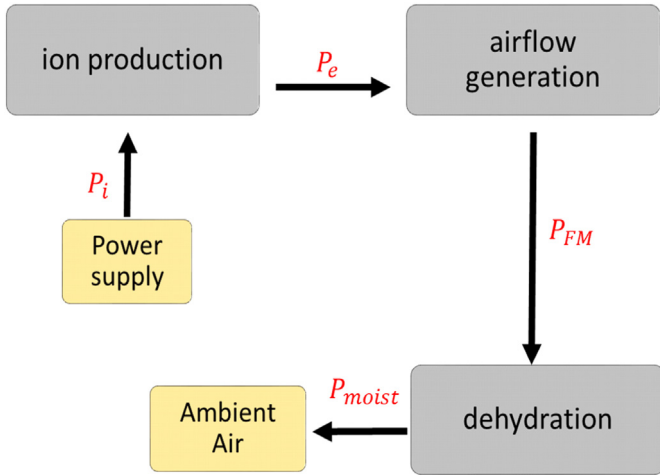


Fig. 3. Schematic illustration of different stages in EHD drying with their inputs and outputs.

thermal radiation, sound/light emission, and all the other losses associated with energy transfer from accelerated charged particles to the airflow. This efficiency index, called here as fluid mechanic exergy efficiency, can be defined as follows:

$$\eta_{FM} = \frac{P_f}{P_e} \times 100\% \quad (17)$$

where P_f is flow power (kinetic exergy) and, as defined for the

pump, $P_f = Q(\delta P)$, where δP [Pa] is the pressure difference generated between the emitter and collector and Q [$\text{m}^3 \text{s}^{-1}$] is air flow rate. Using the dynamic pressure definition, it is possible to rewrite the equation as $P_f = 0.5\rho_a A u^3$, where A [m^2] is the cross-section area of the inlet. It is noteworthy that due to the high amount of losses in this sub-process, the value obtained for this parameter is very small. Third, the drying performance of the device should be considered in the overall performance evaluation which leads us to drying exergy efficiency;

$$\eta_{drying} = \frac{P_{moist}}{P_f} \times 100\% \quad (18)$$

where P_{moist} is the moisture removal exergy (power) derived from the Gibbs free energy equation, which is the energy associated with a chemical reaction. Using the formulation provided in Refs. [26], but for steady conditions, the following formula is considered for P_{moist} .

$$P_{moist} = \frac{m_{moist} (h_{fg} - T_0 S_{fg})}{t_{crit}} \quad (19)$$

Where m_{moist} [kg] is the total removed moisture from the sample during drying time until t_{crit} . T_0 [K] is the ambient temperature, while h_{fg} [J kg^{-1}] and S_{fg} [$\text{m}^2 \text{s}^{-2} \text{K}^{-1}$] are the specific enthalpy and entropy of water evaporation, respectively. Each one of these performance indicator numbers can be used as a powerful tool for analyzing the EHD drying process, as will be seen in section 3. Finally, the overall exergy efficiency ($\eta_{overall}$) can be calculated by

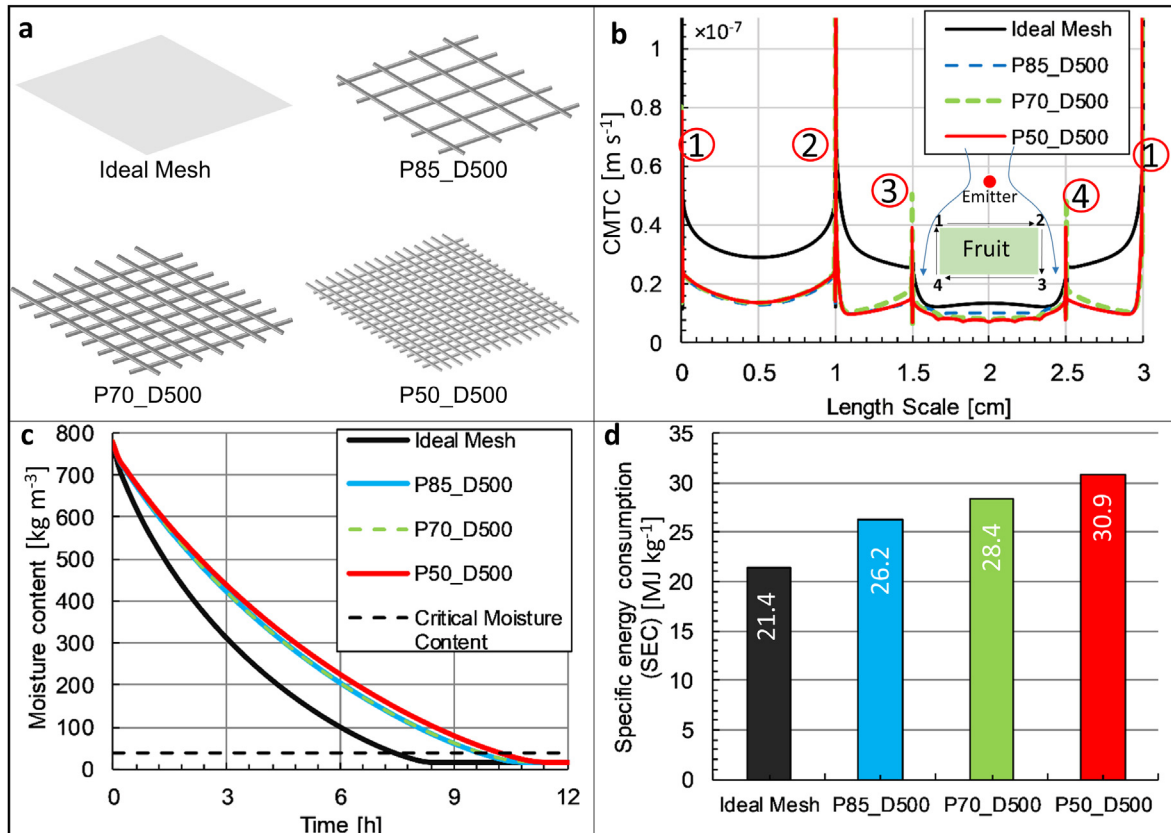


Fig. 4. Simulation of mesh with different open area: a) Illustration of different mesh open areas, b) CMTC as a function of sample boundary length, c) Sample moisture kinetics, d) Specific energy consumption.

multiplying η_E , η_{FM} , and η_{drying} . Fig. 3 represents different sub-processes with related input-output powers that are used in our exergy analysis.

3. Results and discussion

The convective dehydration process at the fruit surface is driven by the airflow field, which is produced by the ionic wind. The produced ionic wind is, in turn, driven by the Coulomb force, which is the result of the electrostatic field and ion concentration in the air. In this section, we will follow the aforementioned chain of events to interpret the results.

3.1. Mesh parameters impact

The main goal of this section is to evaluate the influence of wire diameter and mesh open area on the food drying performance in

terms of energy consumption and drying time.

3.1.1. Ideal mesh vs. real mesh

The difference between an ideal mesh and a mesh where the wires are modeled discretely, is discussed in this section. The drying curves, CMTC value on the air–fruit interface, and the energy consumption are depicted in Fig. 4. In order to have a quantitative evaluation, the most important parameters such as t_{crit} , airspeed, and the average value of Coulomb force, SCD, and electric field in the ROI are calculated (Table 3). The distribution of electrically-related parameters, together with the resulting airspeed distribution, in the region of interest are shown for ideal and real mesh in Fig. 5 and Fig. 6, respectively.

According to Table 3, the average values of the electrostatic and ion-flow parameters for ideal and real meshes, namely electric field intensity, SCD, and Coulomb force, are almost similar. The ideal mesh, however, induces a higher average airspeed around the fruit

Table 3

Quantitative evaluation of the most important parameters for different mesh open areas.

Parameter Case	t_{crit} [h]	Average CMTC [m s^{-1}] $\times 10^7$	Maximum air speed [m s^{-1}]	Average airspeed ^a [m s^{-1}]	Pressure drop ^b [Pa]	Average F_e ^a [N]	Average E^a [V m^{-1}] $\times 10^{-5}$	Average SCD ^a [C m^{-3}] $\times 10^5$
Plate collector	16.25	0.7	2.1	0.63	1.18	23.39	2.64	8.84
Ideal Mesh	7.47	2.6	2.3	0.67	0.02	20.30	2.55	7.96
P85_D500	9.72	1.31	3.2	0.57	0.14	21.12	2.57	8.22
P70_D500	9.75	1.30	3.3	0.57	0.14	21.57	2.59	8.33
P50_D500	10.20	1.28	3.4	0.59	0.25	21.60	2.59	8.34

^a in the region of interest.

^b average over the entire domain.

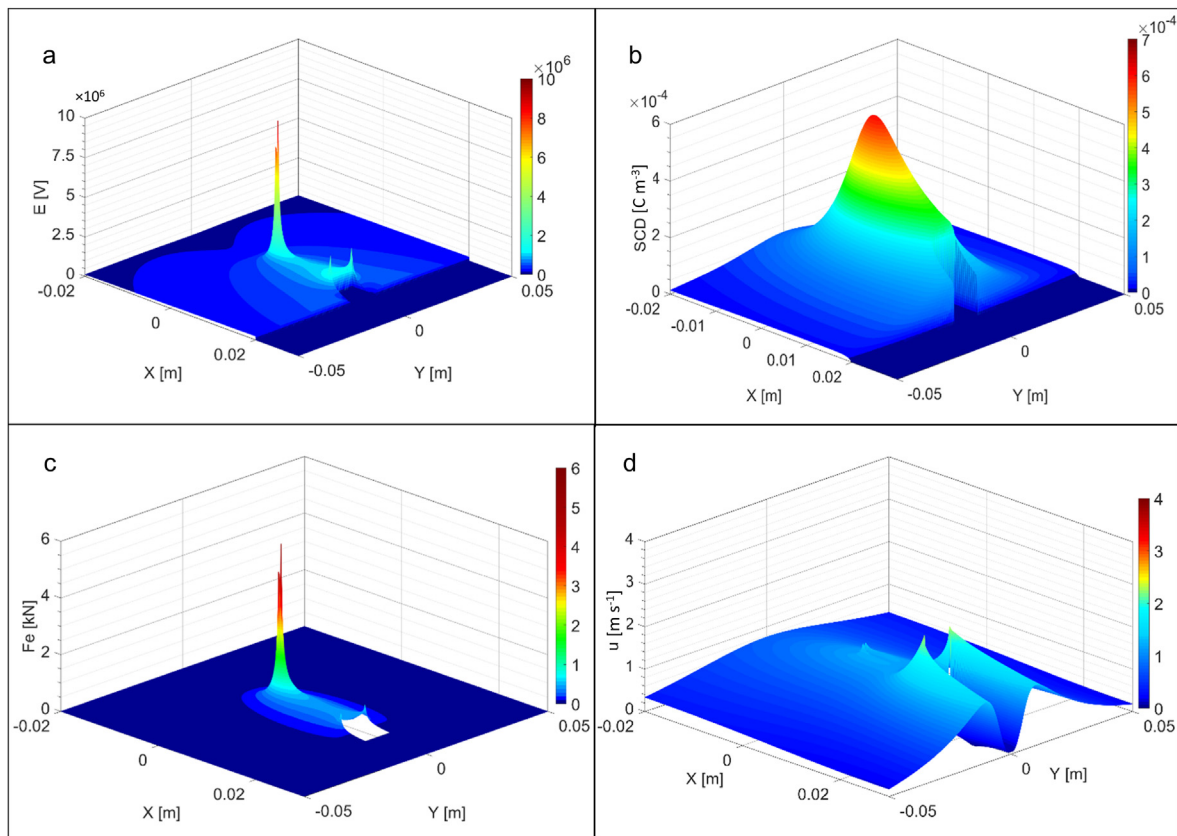


Fig. 5. Distribution of ion flow and electrostatic parameters together with the resulting airspeed in the region of interest for ideal mesh: a) electric field intensity distribution, b) ion (SCD) distribution, c) Coulomb force distribution; d) airspeed distribution.

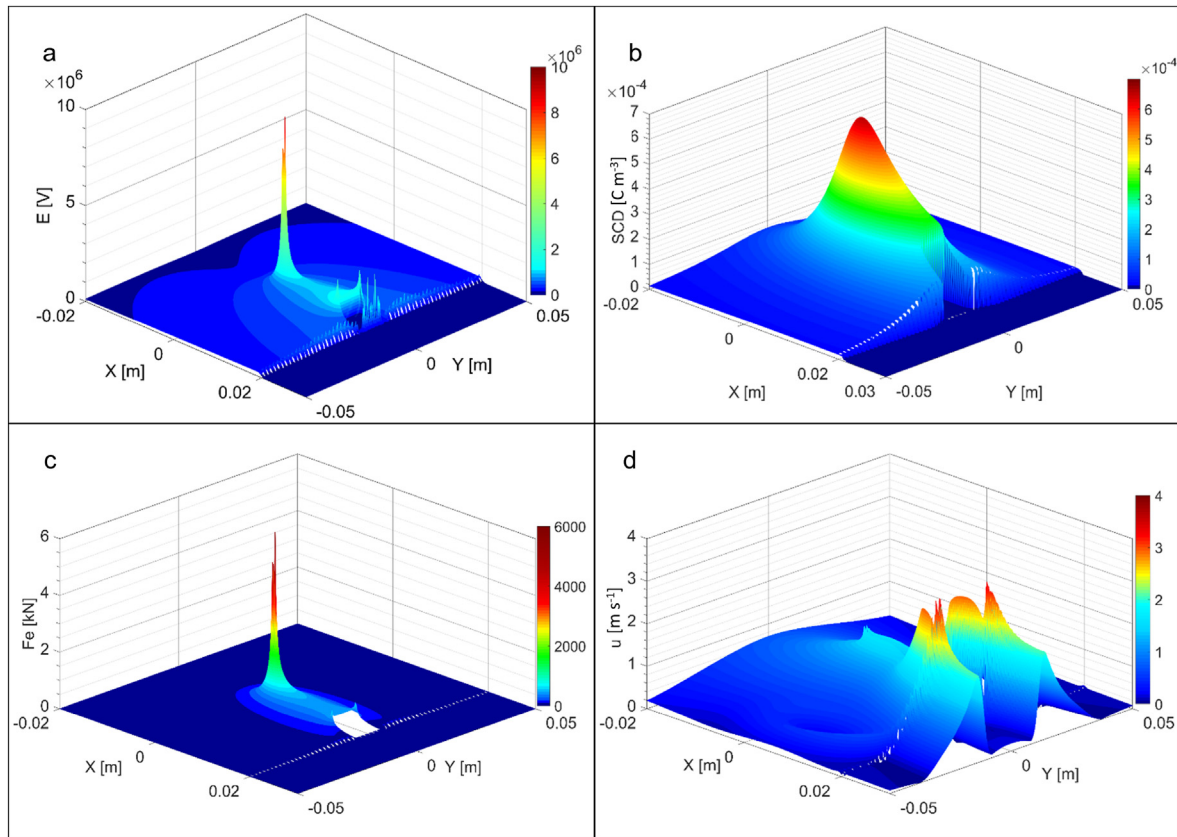


Fig. 6. Distribution of ion flow and electrostatic parameters together with resulting airspeed in the region of interest for P50_D500: a) electric field intensity distribution, b) ion (SCD) distribution, c) Coulomb force distribution; d) airspeed distribution.

(Table 3) and a better drying from the bottom (Fig. 4b). As a result, drying on real mesh is 30% slower than on ideal mesh, with more than a 2-h difference since the real mesh induces a smaller CMTC (Fig. 4b). Dissimilarity in the CMTC between ideal mesh and real mesh arises from a different airflow distribution around the drying material. As it is shown in Figs. 5d and 6d, ideal mesh results in a more uniform airflow around the fruit which improves the moisture removal from the material-air interface. In the real mesh (Fig. 6), a less average airspeed with a higher spatial gradient, compared to the ideal mesh, is generated which leads to a lower moisture removal rate from the material surface. Differences in the flow field (higher average airspeed) and drying characteristics between the ideal and real meshes are attributed to two factors. First, although the average electrostatic and ion-flow parameters are similar, their distribution in the domain is different, which can induce a different flow field. Second, the different pressure drop due to the wires also affects the airflow. The pressure drop over the real mesh was calculated as 0.15 Pa versus 0.02 Pa for the ideal mesh (including the fruit slice). This difference results in smaller average airspeeds and lower CMTC for a real mesh and, hence, a lower drying rate. In summary, we found an added value of modeling the wires discretely in our simulations, compared to in an idealized way. It should be noted, that mesh collector provides fruit drying faster and more uniform than a solid plate collector (Table 3), which is the main advantage of a mesh collector configuration.

3.1.2. Mesh open area effect

In this section, the impact of different mesh open area (50%, 70%, and 85%) with similar wire diameter on the drying kinetics is

evaluated (Fig. 4a). There is no doubt that the mesh open area affects airflow distribution [26,27]. The aim here is to see how this airflow distribution at mesh collector with different open areas would affect the drying kinetics.

The simulation showed that all configurations with different open areas resulted in almost the same drying behavior with negligible differences in drying rate and t_{crit} (Fig. 4c). This surprising finding could be explained by the coupling of aerodynamic and electrostatic effects. From purely aerodynamic considerations, decreasing the mesh open area would increase the pressure drop [27,28]. In a mesh collector, however, the additional effect of electrostatic conditions plays a significant role. Smaller open area corresponds to a stronger average electric field and a larger concentration of ions (charges), leading to a higher average Coulomb force (Table 3). In turn, this leads to an increase in airspeed, especially around the wires. It follows that aerodynamic and electrostatic effects compensate each other, resulting in similar average airspeeds for mesh collectors with different open areas. However, if we compare the specific energy consumptions (Fig. 4d), the effect of the mesh open area becomes significant. By increasing the open area, the energy consumption per unit mass of evaporated water decreases. In the practical context, the industrial design of mesh collector should pursue the largest possible open area, because it would reduce energy consumption without a significant effect on drying time.

3.1.3. Wire diameter effect

The effect of the wire diameter on the drying kinetics was investigated for meshes with the same open area. The wire diameter determines the curvature of the collector electrode, which

Table 4

Quantitative evaluation of the most important parameters for different wire diameters.

	t_{crit} [h]	Average CMTC [m s ⁻¹] × 10 ⁷	Maximum Airspeed [m s ⁻¹]	Average Airspeed ^a [m s ⁻¹]	Average F_e^a [N]	Average E^a [V m ⁻¹] × 10 ⁻⁵	Average SCD ^a [C m ⁻³] × 10 ⁵
P85_D1000	9.56	19.8	2.8	0.56	20.73	2.56	8.10
P85_D500	9.72	19.2	3.2	0.57	21.15	2.57	8.22
P85_D300	9.58	19.7	2.9	0.58	21.23	2.57	8.25
P85_D240	9.46	21.9	3.2	0.59	21.16	2.58	8.20

^a in the region of interest.

affects the electrohydrodynamics. The most important parameters of the different physical processes are shown in Table 4. The smallest wire diameter that was modeled in this study was 240 μm. A lower value is not common for metallic meshes due to the problems with manufacturing and structural strength considerations. Although the impact of wire diameter on the drying time is not very striking, a smaller wire diameter generally leads to higher average airspeeds, CMTCs and drying rates. The absence of a clear correlation between wire diameter and process parameters could be explained by the resulting difference in the distributions of the electric field, ion flow and, subsequently, the Coulomb force and airflow field.

3.1.4. Energy analysis

In this section, mesh open area and wire diameter effects are evaluated with respect to energy consumption. The quantified power used by each sub-process is tabulated in Table 5. The discharge power (P_e) slightly increases by decreasing the open area due to the larger overall collector surface, which leads to a higher ionic (charge) current. The impact of the wire diameter on P_e shows different behavior in high (85%), medium (70%), and low (50%) open area meshes. In high open area meshes (85%), collector wires with a smaller diameter induce a higher discharge power due to the higher curvature of the collecting surfaces. In low open area meshes, the wire spacing in the mesh collector is very small. This seems to affect the electric field in such a way that a higher curvature of the wires does not increase the electric field intensity around the wires.

Flow power (P_f) is determined by pressure drop on the mesh. A smaller open area results in a higher pressure drop and, consequently, lower flow power. For meshes with large open areas, the pressure drag increases with the increase of wires density per unit area (or decrease of wire diameter). In contrast, for meshes with small open areas, the effect is the opposite. Spacings smaller than 5 wire diameters increase the pressure drop due to the additional interference drag combined with the individual pressure drag of

each wire [29]. On the other hand, a smaller open area increases the overall collector surface, which results in a higher ionic current hence, higher Coulomb force and energy consumption. As already mentioned, this higher Coulomb force compensates the higher pressure drop to some extent, therefore keeps the drying rate almost constant for different open areas.

The power required for dehydration (P_{moist}) for different open areas and wire diameter is almost the same, which results in the same drying time for all cases. Overall, the total energy consumption, as mentioned before, increases by decreasing the mesh open area.

3.1.5. Exergy analysis

In this section, different exergy efficiency indices are evaluated to identify the source of losses and opportunities for energy efficiency improvement in the EHD dryer system. Energy analysis is useful to show the energy consumption and required power for different parts of the system. However, it gives no information about how far a given system is from ideal conditions. This can be done with exergy analysis.

The electrical exergy efficiency (η_E) has a direct relation with the overall collector surface (Table 5). Accordingly, the highest value of η_E is associated with an ideal mesh that has the maximum possible collector surface. Hence, the smaller the open area, the higher the collector surface and the lower the ion production losses. The high values of η_E shows that ion-production sub-process contains very low losses, so there is a very limited opportunity for further improvement. Note that usually the input power for electrical efficiency calculation is considered as the input power of the power supply device. In the current calculations, input power is considered as the discharge power at the emitter so the losses in the power supply are not included; therefore, we can see high values for η_E in the Table 5. These values would be lower in a real situation and can be improved by increasing the power supply efficiency.

Fluid mechanic exergy efficiency (η_{FM}) is the smallest compared with other exergy efficiencies. Obviously, a large share of the total

Table 5

Calculations of power and exergy efficiency for different mesh open areas and wire diameters.

Parameter Case	Number of released electrons × 10 ⁻¹⁵	Input power P_i [W]	Discharge power P_e [W]	Flow power P_f [W] × 10 ³	Moisture removal power P_{moist} [W] × 10 ³	Electrical exergy efficiency η_E [%]	Fluid mechanic exergy efficiency η_{FM} [%]	Drying exergy efficiency η_{Drying} [%]	Overall exergy efficiency $\eta_{overall}$ [%]
Plate collector	11.5	36.7	36.6	17.2	4.9	99.7	0.05	28.4	0.01
Ideal Mesh	9.7	31.1	30.7	19.9	10.6	98.8	0.06	53.3	0.03
P85_D1000	8.6	27.5	26.2	39.8	8.3	95.3	0.15	20.8	0.03
P85_D500	9.1	29.2	28.3	45.9	8.2	97.0	0.16	17.8	0.03
P85_D300	9.4	30.2	29.4	54.2	8.3	97.5	0.18	15.3	0.03
P85_D240	9.4	30.2	29.5	52.9	8.3	97.6	0.18	15.6	0.03
P70_D1050	10.0	32.2	31.4	44.6	8.2	97.6	0.14	18.3	0.03
P70_D500	9.9	31.7	31.1	43.3	8.1	98.1	0.14	18.6	0.03
P50_D1900	11.0	35.3	34.6	49	8.0	98.0	0.14	16.4	0.02
P50_D900	10.5	33.9	33.2	40.2	8.2	98.3	0.12	20.4	0.02
P50_D500	10.2	32.7	32.3	31.4	7.8	98.7	0.10	24.66	0.02

losses in the system is dedicated to momentum transfer from ions to the neutral air particles. Therefore, there is a large opportunity for performance improvement and further optimization of this sub-process. Note that a higher η_{FM} means that a higher amount of the potentially available momentum that is provided by accelerated ions is exploited.

In the last sub-process (moisture removal), the drying exergy efficiency (η_{Drying}) decreases by a factor of 2 for the real mesh when the wires are modeled discretely. Based on this difference between ideal and real mesh, further improvement in this sub-process is also possible. Because the current model considers only convective dehydration, improvements in aerodynamic conditions have to be pursued. Hence, in the optimization process, we tried to have an airflow distribution similar to the ideal mesh by proper arrangement of grounded wires. Finally, considering $\eta_{overall}$, the very open mesh is the best option for the mesh collector configuration. Further optimization (next part of the current study) should be done through both aerodynamic and electrostatic considerations in order to improve η_{Drying} and η_{FM} , respectively.

3.2. Mesh collector optimization

Employing a mesh as the collector opens up opportunities for manipulations of electrostatic conditions and ionic flow distribution, which is another advantage of a mesh over plate collector. The mesh collector gives better flexibility to alter Coulomb force distribution via grounding wires in specific locations. Based on the insights obtained from the previous section, this section aims to optimize mesh configuration in terms of high drying rate and low energy consumption by improving η_{FM} and η_{Drying} . The reason for the improvement was our ability to change the Coulomb force distribution by manipulating electric field intensity, the space charge density, and their distributions. The resulting Coulomb force is supposed to provide relatively high average airspeed and airflow distribution close to the ideal case by which η_{Drying} will increase. The results of this optimization are described and discussed in the following sections.

3.2.1. Optimization of the active area of the collector electrode

As the first step in our optimization study, the optimal active area of the collector electrode (i.e. number of the grounded wires) was explored. The mesh with 85% open area (namely, P85_D240) was selected for this optimization based on its best performance among other configurations (see section 3.1). Fig. 7 shows the graphs used for the performance evaluation of different cases. The results for the highest gradient region in Fig. 7c are shown, in Fig. 7d, to have a better resolution. In Fig. 7d, the configurations which have at least one wire in contact with the sample are shown by hollow circles. Because the fruit has some conductivity, when it is in contact with the grounded wires, it acts partially like a collector surface (especially in its sharp corners) and increases the overall collector surface. As such, it also affects the electric field and ion flow distribution. Therefore, the cases where the wires are in contact with the sample have to be distinguished from the others.

Based on the specific energy consumption graph (Fig. 7a), the higher the number of grounded wires, the higher the energy consumption due to the higher ionic current (the applied voltage is constant for all cases). The critical drying time in Fig. 7b reaches an asymptote for more than four grounded wires. P85_1wire and P85_2wire configurations cannot be among the optimal options due to the huge difference in drying time compared with other configurations. Based on Fig. 7c and d the mesh configuration with 4 grounded wires shows the best overall exergy efficiency. Considering the trade-off between drying time, energy consumption, and exergy efficiency, the optimal number of grounded wires is four when none of the grounded wires are in contact with the fruit. When the grounded wires are in contact with the fruit surface, the electrical conductivity of the fruit makes the fruit to act as a grounded surface to some extent. This situation changes the electrostatic conditions and creates a different $\eta_{overall}$ as a function of the number of wires (Fig. 7d).

In Table 6 the values of convective drying exergy efficiency (η_{Drying}) for P85_1wire and P85_2wire are considered as zero because the generated airflow is very weak which results in almost natural dehydration. The number of released electrons during

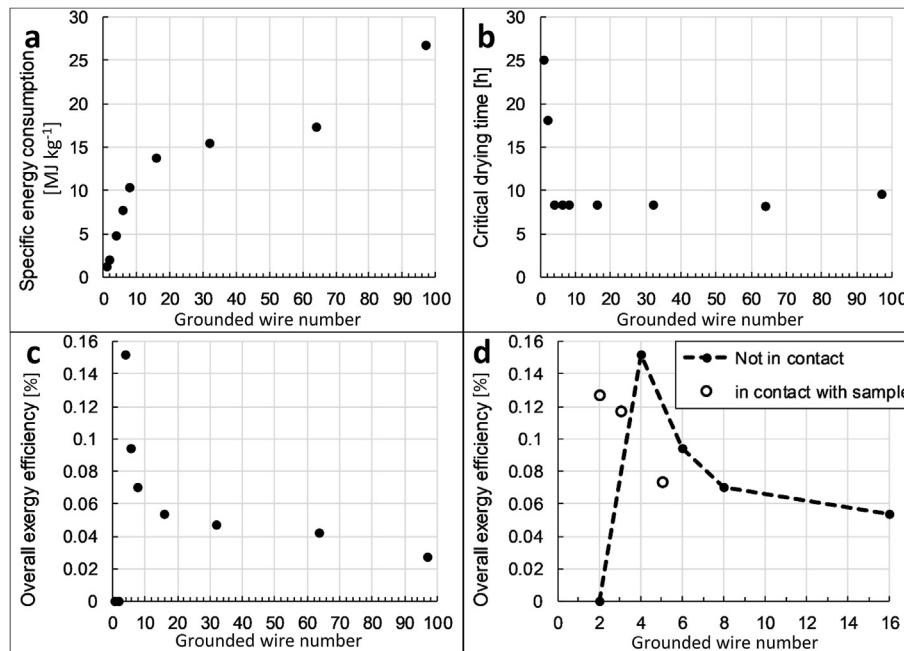


Fig. 7. Optimization based on performance indicator graphs for different grounded wire numbers: a) Specific energy consumption, b) Drying time, c) Exergy efficiency, d) Exergy efficiency of the best configurations.

Table 6

Calculations of exergy efficiency and overall performance for different number of grounded wires.

Parameter Case name	Number of released electron $\times 10^{-15}$	Input power P_i [W]	Discharge power P_e [W]	Flow power P_f [W] $\times 10^3$	Moisture removal power P_{moist} [W] $\times 10^3$	Electrical exergy efficiency η_E [%]	Fluid mechanic exergy efficiency η_{FM} [%]	Drying exergy efficiency η_{Drying} [%]	Overall exergy efficiency $\eta_{Overall}$ [%]
P85_1wire	0.17	0.5	0.5	0.0	3.2	86.8	0.0	0	0
P85_2wire	0.39	1.2	1.1	0.5	4.4	86.7	0.0	0	0
P85_2wire_Contact	2.35	7.5	6.8	38.6	9.6	89.9	0.6	24.9	0.13
P85_3wire_Contact	2.55	8.2	7.3	38.3	9.6	89.2	0.5	25.0	0.12
P85_4wire	1.96	6.3	5.4	38.3	9.5	86.9	0.7	24.9	0.15
P85_5wire_Contact	4.09	13.1	11.0	38.6	9.6	84.0	0.3	25.0	0.07
P85_6wire	3.15	10.1	9.0	39.7	9.5	89.3	0.4	24.0	0.09
P85_8wire	4.20	13.6	12.3	39.4	9.5	90.4	0.3	24.2	0.07
P85_16wire	5.56	17.8	16.3	40.1	9.5	91.7	0.2	23.7	0.05
P85_32wire	6.28	20.1	18.5	38.4	9.5	92.0	0.2	24.8	0.05
P85_64wire	7.11	22.8	21.2	38.5	9.6	93.1	0.2	25.0	0.04

corona discharge for P85_4wire (Table 6) is approximately five times lower than not-optimized meshes (Table 5). Taking into account the chemical reaction chains happening in the corona discharge provided in Ref. [30,31] this leads to five times lower toxic gas (Ozone and NOx) emissions, which is very important for an environmentally friendly device.

3.2.2. Optimization of the location of the grounded wires

The second step in the optimization study is to optimize the spacing of those four grounded wires. The results of the location optimization procedure are shown in Fig. 8. Fig. 8a and b show the schematic of the locations of the grounded wires and the naming system used for these case studies. Fig. 8c shows the drying curve of

the optimized configurations. In the best case that we could reach (Fig. 8d and e), four collector wires were located at $d_1 = \pm 1.1L_s$ and $d_2 = \pm 0.6L$ (Fig. 8a). The overall exergy efficiency ($\eta_{Overall}$) for P85_4wire_1.1_0.6 is increased to 0.20% which shows 30% improvement compared with the standard case (P85_4wire). Moreover, comparing the drying curves of P85_4wire_1.1_0.6 and P99_4wire_1.1_0.6 shows the effect of pressure drop on the drying rate due to decreasing the mesh open area.

The difference in electrostatic parameters and ion density distribution between the optimized case and the other studied configurations is shown in Fig. 9. The difference in the SCD and electric field distributions for different configurations results in an obvious difference in Coulomb force distribution between the optimized

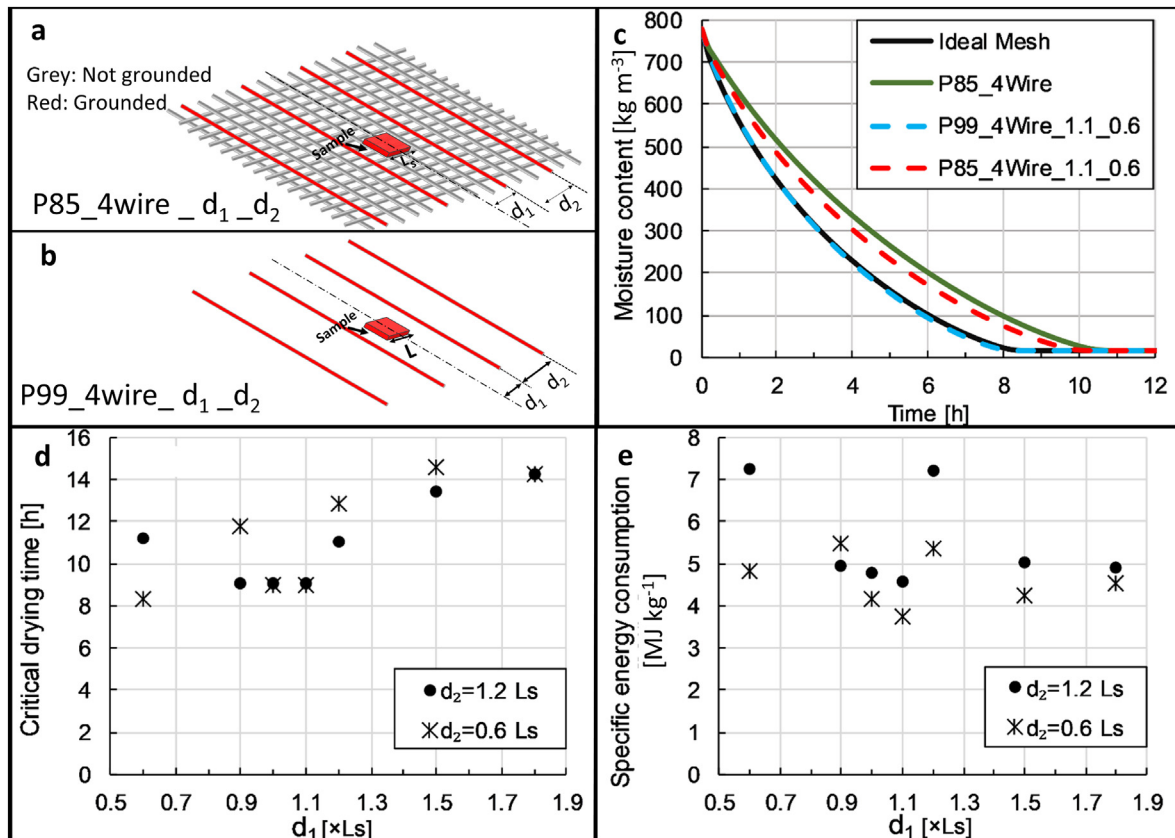


Fig. 8. a) and b) Schematic illustration of optimized configuration, c) Drying curves for comparing optimized configuration with other configurations d) airspeed distribution in ROI for ideal mesh, e) airspeed distribution in ROI for optimized configuration.

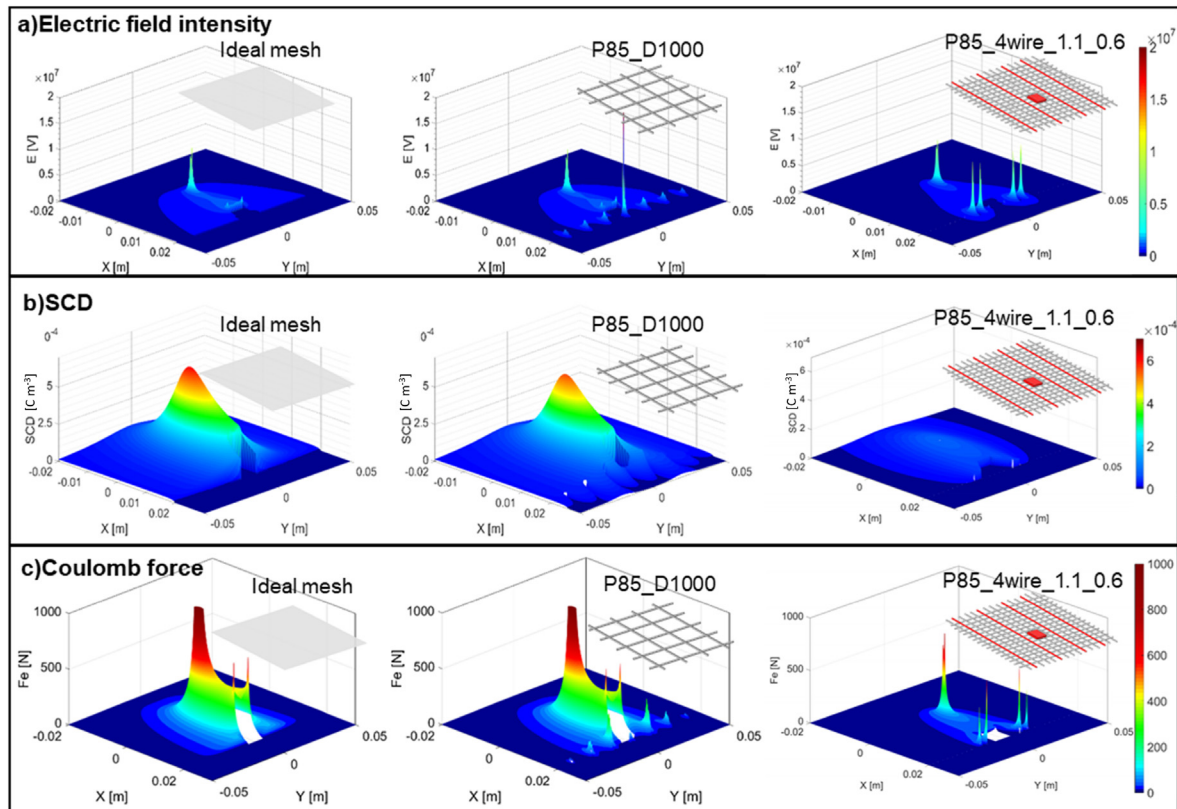


Fig. 9. Distribution of ion density and electrostatic parameters in ROI: a) Electric field intensity distribution b) SCD and ionic current distribution, c) Coulomb force distribution.

case and the other configurations. As a result of the manipulation of the electric field in the region of interest, with an even lower average SCD and F_e , a satisfactory average airspeed is reached just by proper arrangement of the grounded wires which increases the fluid mechanic exergy efficiency. The resulting airspeed together with the airflow distribution around the sample (low-pressure drop behind mesh and fruit) leads to relatively good drying time with low energy consumption. The specific energy consumption of the optimal configuration during the drying time is more than 7 times lower than other configurations (Fig. 10). This is a huge improvement and a step toward a more efficient EHD drying

device. This configuration can be proposed for further experimental validations.

4. Conclusion

In this study, we optimized in-silico a mesh collector design of an electrohydrodynamic fruit dryer in order to significantly reduce its energy consumption. This design was optimized by targeting drying time and energy consumption while analyzing the exergy of ion generation, momentum transfer to air, and dehydration. Our main conclusions are:

- The geometrical parameters of the mesh, namely wire diameter and open area, do not influence the dehydration kinetics significantly. However, the energy consumption increases with decreasing the open area of the mesh. Hence, to minimize drying time and minimize energy consumption, the mesh open area should be chosen as large as possible.
- An optimized mesh configuration is designed, which provides a similar drying time but a seven times lower energy consumption compared with a standard mesh.

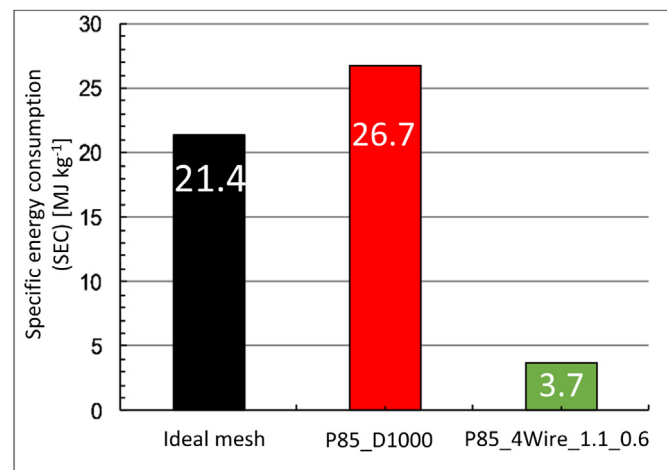


Fig. 10. Specific energy consumption for an ideal mesh, a mesh where the wires are discretely modeled and such a mesh that is optimized.

This research demonstrated another advantage of the mesh collector over the plate collector. Using a mesh as a collector provides the opportunity for the manipulation of the electrostatic parameters and ion flow. By having a proper analysis of the electrostatic and aerodynamic conditions, it is possible to reach an optimal configuration of the collector wires. With this study, we made this upscalable EHD dryer design now much more energy-efficient, which paves the way to industrial prototypes and pilot plants.

Author statement

T. Defraeye conceptualized the study and did project administration; T. Defraeye wrote the project proposal, secured the funding; K. Iranshahi and T. Defraeye developed the methodology; K. Iranshahi performed the CFD simulations; K. Iranshahi performed analysis, interpretation of the results; T. Defraeye performed supervision of K. Iranshahi. K. Iranshahi wrote the original draft with key inputs of T. Defraeye; T. Defraeye and A. Martynenko critically reviewed and edited the manuscript, and K. Iranshahi revised the manuscript on the basis of these suggestions.

Declaration of competing interest

The authors declare that they have no known competing financial interests or personal relationships that could have appeared to influence the work reported in this paper.

Acknowledgment

We would like to thank Prof. Dr. Paolo Gaetani (Politecnico di Milano, department of energy), for the co-supervision of the first author during his master project. The authors also acknowledge the ETH Foundation and the World Food System Center of ETH Zurich for supporting this project.

References

- [1] Lamidi RO, Jiang L, Pathare PB, Wang YD, Roskilly AP. Recent advances in sustainable drying of agricultural produce: a review. *Appl Energy* 2019;233–234:367–85. <https://doi.org/10.1016/j.apenergy.2018.10.044>.
- [2] Lin Tm D, Durand T, Scaman CH. Characterization of vacuum microwave, air and freeze dried carrot slices. *Food Res Int* 1998;31:111–7. [https://doi.org/10.1016/S0963-9969\(98\)00070-2](https://doi.org/10.1016/S0963-9969(98)00070-2).
- [3] Gunasekaran S. Pulsed microwave-vacuum drying of food materials. *Dry Technol* 1999;17:395–412. <https://doi.org/10.1080/07373939908917542>.
- [4] Jeyamkondan S, Jayas DS, Holley RA. Pulsed electric field processing of foods: a review. *J Food Protect* 1999;62:1088–96. <https://doi.org/10.4315/0362-028X-62.9.1088>.
- [5] Liapis A, Marchello J. *Advances in the modeling and control of freeze-drying*, vol. 3. Hemisphere Publishing; 1984.
- [6] Chen XD, Mujumdar AS. *Drying technologies in food processing*. Wiley-Blackwell; 2008.
- [7] Atungulu GG. *High electric field technology in post harvest drying*. Fresh prod, vol. 1. Global science book; 2007. p. 23–31.
- [8] Onwude DI, Hashim N, Janius RB, Nawi NM, Abdan K. Modeling the thin-layer drying of fruits and vegetables: a review. *Compr Rev Food Sci Food Saf* 2016;15:599–618. <https://doi.org/10.1111/1541-4337.12196>.
- [9] Martynenko A, Kudra T. Electrohydrodynamic (EHD) drying of grape pomace. *Japan J Food Eng* 2016;17:123–9. <https://doi.org/10.11301/jsfe.17.123>.
- [10] Defraeye T, Martynenko A. Electrohydrodynamic drying of food: new insights from conjugate modeling. *J Clean Prod* 2018;198:269–84. <https://doi.org/10.1016/j.jclepro.2018.06.250>.
- [11] Bajgai TR, Raghavan GSV, Hashinaga F, Ngadi MO. Electrohydrodynamic drying – a concise overview. *Dry Technol* 2006;24:905–10. <https://doi.org/10.1080/07373930600734091>.
- [12] Iranshahi K, Mani M. Dielectric barrier discharge actuators employed as alternative to conventional high-lift devices. *J Aircraft* 2018;55:1–10. <https://doi.org/10.2514/1.C034690>.
- [13] Lai FC. A prototype of EHD-enhanced drying system. *J Electrostat* 2010;68:101–4. <https://doi.org/10.1016/j.elstat.2009.08.002>.
- [14] Misra NN, Martynenko A, Chemat F, Paniwnyk L, Barba FJ, Jembrak AR. Thermodynamics, transport phenomena, and electrochemistry of external field-assisted nonthermal food technologies. *Crit Rev Food Sci Nutr* 2018;58:1832–63. <https://doi.org/10.1080/10408398.2017.1287660>.
- [15] Defraeye T, Martynenko A. Electrohydrodynamic drying of multiple food products: evaluating the potential of emitter-collector electrode configurations for upscaling. *J Food Eng* 2019;240:38–42. <https://doi.org/10.1016/j.jfoodeng.2018.07.011>.
- [16] Martynenko A, Kudra T. Electrically-induced transport phenomena in EHD drying – a review. *Trends Food Sci Technol* 2016;54:63–73. <https://doi.org/10.1016/j.tifs.2016.05.019>.
- [17] Martynenko A, Astatkie T, Riaud N, Wells P, Kudra T. Driving forces for mass transfer in electrohydrodynamic (EHD) drying. *Innovat Food Sci Emerg Technol* 2017;43:18–25. <https://doi.org/10.1016/j.ifset.2017.07.022>.
- [18] Barlow JB, Rae WH, Pope A. *Low speed wind tunnel testing*, vol. 7. Wiley & Sons Ltd.; 1999.
- [19] Jewell-Larsen NE, Karpov SV, Krichitavovitch IA, Jayanty V, Hsu C-P, Mamishev AV. Modeling of corona-induced electrohydrodynamic flow with COMSOL multiphysics. *Minneapolis, Minnesota: ESA Annu. Meet. Electrostat*; 2008.
- [20] Defraeye T, Verboven P. Convective drying of fruit: role and impact of moisture transport properties in modelling. *J Food Eng* 2017;193:95–107. <https://doi.org/10.1016/j.jfoodeng.2016.08.013>.
- [21] Shrimpton J. *Charge injection systems*. Berlin, Heidelberg: Springer Berlin Heidelberg; 2009. <https://doi.org/10.1007/978-3-642-00294-6>.
- [22] Rosen MA. Assessing energy technologies and environmental impacts with the principles of thermodynamics. *Appl Energy* 2002;72:427–41. [https://doi.org/10.1016/S0306-2619\(02\)00004-1](https://doi.org/10.1016/S0306-2619(02)00004-1).
- [23] Chow TT, Pei G, Fong KF, Lin Z, Chan ALS, Ji J. Energy and exergy analysis of photovoltaic-thermal collector with and without glass cover. *Appl Energy* 2009;86:310–6. <https://doi.org/10.1016/j.apenergy.2008.04.016>.
- [24] Aghbashlo M, Mobli H, Rafiee S, Madadlou A. A review on exergy analysis of drying processes and systems. *Renew Sustain Energy Rev* 2013;22:1–22. <https://doi.org/10.1016/j.rser.2013.01.015>.
- [25] Sciubba E, Wall G. *A brief commented history of exergy from the beginnings to*, vol. 10; 2004. 2007.
- [26] Bardy E, Hamdi M, Havet M, Rouaud O. Transient exergetic efficiency and moisture loss analysis of forced convection drying with and without electrohydrodynamic enhancement. *Energy* 2015;89:519–27. <https://doi.org/10.1016/j.energy.2015.06.017>.
- [27] Laws EM, Livesey JL. Flow through screens. *Annu Rev Fluid Mech* 1978;10:247–66. <https://doi.org/10.1146/annurev.fl.10.010178.001335>.
- [28] Brundrett E. Prediction of pressure drop for incompressible flow through screens. *J Fluid Eng* 1993;115:239. <https://doi.org/10.1115/1.2910130>.
- [29] Zdravkovich MM. REVIEW—review of flow interference between two circular cylinders in various arrangements. *J Fluid Eng* 1977;99:618–33. <https://doi.org/10.1115/1.3448871>.
- [30] Fridman A. *Plasma Chemistry*. Cambridge: Cambridge University Press; 2008. <https://doi.org/10.1017/CBO9780511546075>.
- [31] Morent R, Leys C. Ozone generation in air by a DC-excited multi-pin-to-plane plasma source. *Ozone Sci Eng* 2005;27:239–45. <https://doi.org/10.1080/01919510590945813>.